ORIGINAL PAPER

CrossMark

Does the low optical band gap of yellow Bi_3YO_6 guarantee the photocatalytical activity under visible light illumination?

K. Trzciński[1] · M. Szkoda[1] · A. Herman[2] · A. Borowska-Centkowska[3] · A. Lisowska-Oleksiak[1]

Abstract

Bi_3YO_6, which is known as an ionic conductor, was tested here as an electrode and photoanode in contact with aqueous electrolytes. Bi_3YO_6 was deposited onto the Pt substrate and the such prepared electrode was polarized in various aqueous electrolytes. The optical energy band gap of the material equal to 1.89 eV was determined using the Kubelka-Munk function resulting from the UV-Vis spectrum (allowed indirect transition) and also was calculated using the semi-empirical PM7 method (3.38 eV of HOMO-LUMO energy gap). Despite the yellow color of Bi_3YO_6, the tested material exhibits photoelectroactivity only in the UV range of electromagnetic radiation. The anodic photocurrent characteristic for n-type metal oxide semiconductors was recorded. The electrode exhibits diffusion-controlled cathodic activity while polarized in chloride-free aqueous electrolytes.

Keywords Bi_3YO_6 · Semiconductor · Aqueous electrolyte · Photoactivity · Photoanode

Introduction

Metal oxides are known to be used in many electrochemical-based devices such as gas sensor, biosensor, and chemical sensor [1], optical sensors [2], lithium ion batteries [3], photoanodes [4], and environmental remediation photocatalysts [5]. A group of bismuth inorganic compounds such as Bi_2O_3, $BiVO_4$, BIMEVOX, $BiMoO_6$, BiOCl, and Bi_2WO_6 are known to act as electrode materials, exhibiting high electrical capacity, chemical stability under multiple polarization cycles, photoelectroactivity, and photocatalytical properties [6–11].

✉ K. Trzciński
kontrzci@pg.edu.pl

✉ A. Lisowska-Oleksiak
alo@pg.edu.pl

1 Faculty of Chemistry, Department of Chemistry and Technology of Functional Materials, Gdansk University of Technology, Narutowicza 11/12, 80-233 Gdansk, Poland

2 Faculty of Chemistry, Department of Inorganic Chemistry, Gdansk University of Technology, Narutowicza 11/12, 80-233 Gdansk, Poland

3 Faculty of Physics, Solid State Ionics Division, Warsaw University of Technology, Koszykowa 75, 00-662 Warsaw, Poland

Their potential applications spread from supercapacitors to photoelectrochemical cells for water splitting or water pollutant degradation. Some of these compounds belong to high temperature solid state electrolytes, having a structure allowing oxygen ions mobility to occur.

The δ-Bi_2O_3 is a high temperature polymorph of bismuth oxide [12]. The significant decrease of ionic conductivity at lower temperatures is observed due to the phase transition of cubic δ-phase to α, β, or γ polymorphs. Great effort has been made to preserve the high-conducting structure at lower temperatures. It can be achieved via partial substitution of Bi atoms in Bi_2O_3 by, e.g., rare earth metals [13], which leads to the formation of a series of new compounds with new properties. One of them is Bi_3YO_6 that occurs in the δ-phase even at room temperature [14]. The defect structure, vacancy ordering, and oxygen ion transport in the Bi_3YO_6 δ-phase were studied using ab initio molecular dynamic, as well as total neutron scattering analysis [15–17]. Ionic transport in a material and its defect structure are commonly tested in Bi_3NbO_7-Bi_3YO_6 systems [18, 19] and in tungsten-doped Bi_3YO_6 [20].

Some of bismuth-containing solid electrolytes which are characterized by high ionic conductivity may exhibit also gas sensing properties [21] or be tested as solid membranes for gas separation [22]. Such materials in contact with aqueous electrolytes may show completely new features. The materials from the Bi_2O_3-V_2O_5-Me_xO_y system (BIMEVOX) are a good

example. It was reported that BIMEVOX layers deposited onto the conductive substrate exhibit photoelectrochemical activity and may be used as photoanodes [8, 23, 24]. The unique electronic structure of Bi-containing oxides characterized by a well spread valence band consisting of Bi 6s and O 2p orbitals makes them good candidates for being visible-light active photocatalysts [25]. Materials in the form of powder were tested also as catalysts active under visible light illumination, able to photodegrade organic contaminations [26, 27] and photoreduce Cr (VI) [28]. Thus, materials which are known as solid electrolytes and exhibit outstanding ionic conductivity should be tested and exploited as semiconductors at low temperatures in contact with aqueous electrolytes. We focus on these compounds which exhibit optical properties, suggesting their activity under visible light illumination in respect to photoelectroactivity—semiconductors with a narrow energy band gap. Such a material is tested here—the yellow in color Bi_3YO_6 double oxide known as a high temperature solid state electrolyte [14].

In the present work, Bi_3YO_6 powder was deposited onto a conductive substrate and tested as an electrode. The influence of electromagnetic radiation on electrochemical performance of prepared electrodes was studied. The films of Bi_3YO_6 on Pt substrate were used as photoanodes for photoelectrocatalytical oxidation of water. The structure, surface, and optical properties were tested using XRD, FT-IR, XPS, and UV-Vis, respectively.

Experimental

Apparatus

Ambient temperature X-ray powder diffraction data were collected on a Philips X'Pert Pro X-ray diffractometer fitted with an X'Celerator detector, using Ni filtered Cu-Kα radiation ($\lambda_1 = 1.54056$ Å and $\lambda_2 = 1.54439$ Å), in flat plate θ/θ geometry on a spinning sample holder. Data collection was carried out the range 5–125° 2θ, in steps of 0.0167°, with an effective scan time of 50 s per step. Calibration was carried out with an external LaB_6 standard.

The UV-Vis spectra of Bi_3YO_6 were recorded using a dual beam UV-Vis spectrophotometer (Lambda 35, Perkin-Elmer) equipped with a diffuse reflectance accessory. FT-IR analyses were carried out by using a Nicolet 8700 FT-IR spectrometer equipped with an attenuated total reflectance (ATR) accessory. The morphology of the Bi_3YO_6 layers was investigated by the Schottky field emission scanning electron microscope (FEI Quanta FEG 250) with an ET secondary electron detector. The beam accelerating voltage was kept at 15 kV. Electrochemical and photoelectrochemical experiments (cyclic voltammetry,

electrochemical impedance spectroscopy, chronoamperometry) were performed using the AutoLab PGStat10 potentiostat–galvanostat system under GPES 4.9 software control. Electrochemical impedance spectroscopy (EIS) measurements were recorded in 0.2 M KCl and 0.1 M K_2SO_4 in the 20 kHz–0.1 Hz frequency range at rest potential. The fitting procedure was performed using EIS spectrum analyzer software. Three types of elements were utilized to prepare the electrical equivalent circuit: R—resistor, CPE—constant phase element, and W_o—Warburg open element (the impedance of finite-length diffusion with reflective boundary).

Impedance of the constant phase element is defined as:

$$Z(\omega) = P^{-1}(j\omega)^{-n} \tag{1}$$

and impedance of the Warburg open element is given by the formula:

$$Z_{Wo}(\omega) = \frac{W_{or}}{\sqrt{\omega}}(1-j)\coth\left[W_{oc}\sqrt{j\omega}\right] \tag{2}$$

Measurements carried out under illumination were performed in a photoelectrochemical cell equipped with a quartz window. The geometrical surface area of the electrodes was equal to ~ 0.5 cm^2. A high-pressure 150-W xenon lamp (Osram XBO 150) with and without the AM1.5 filter was used as a source of electromagnetic radiation. The light intensity was adjusted to 100 mW cm^{-2} (with the AM1.5 filter) and 160 mW cm^{-2} (without the AM1.5 filter) and was controlled by an Ophir power meter. All electrochemical measurements were carried out at room temperature 21 °C. XPS analysis was performed for three Pt/Bi_3YO_6 samples before and after polarization in K_2SO_4 electrolyte using Escalab 250Xi from Thermo Fisher Scientific. In order to normalize spectroscopic measurements, the x axis (binding energy) from the XPS spectrum was calibrated for peak characteristics for carbon 1 s (284.6 eV). Data analysis was performed using Avantage software provided by the manufacturer. One sample was electrooxidized (60 min at $E = 0.9$ V), the second one was electroreduced (60 min at $E = -0.85$ V), and the last one was not polarized.

Chemicals

Li_2SO_4, Na_2SO_4, K_2SO_4, Cs_2SO_4, KCl, and KNO_3 used as electrolytes were of analytical grade and were supplied by POCH. Bi_2O_3 (99.9%) and Y_2O_3 (99.99%) used for material synthesis were supplied by Sigma Aldrich.

Synthesis

Bi_3YO_6 was synthesized by conventional solid state reaction technique. Sample of Bi_3YO_6 was prepared using

stoichiometric amounts of Bi_2O_3 and Y_2O_3. The starting mixtures were ground in ethanol using a planetary ball mill. The dried mixtures were heated at 740°C for 24 h, then slow cooled and reground. The sample was then reheated at 800 °C for further 24 h before slow cooling in air to room temperature, over a period of approximately 5 h.

Electrode preparation

Bi_3YO_6 powder was deposited onto the platinum foil using the dip-coating method. First, 0.2 g of material and about 0.1 g of poly(ethylene oxide—PEO) ($M = 300,000$, Aldrich) were mixed with 1 ml of water. The platinum foil was immersed in the resulting suspension, pulled out, dried, and heated for 5 h at 400 °C in an air atmosphere (with a heating rate of 1 °C min^{-1}). The annealing procedure was performed in a quartz tube using a Czylok PRC 55 L/1300 M furnace.

To avoid contact of the studied material with PEO, some of the electrodes were prepared using a glass capillary filled with Bi_3YO_6, where the Pt wire was used as an electrical contact. To test the influence of binder on the photoelectrochemical properties, some of the electrodes were prepared by dropcasting of the Bi_3YO_6 water suspension on the platinum foil and then dried at 100 °C.

Results

Powder and electrode characterization

SEM

The morphology of the layer, deposited using the proposed method, is dependent on the morphology of the starting powder. Scanning electron micrographs of the Bi_3YO_6 layer are presented in Fig. 1a, b. The method of deposition allows a compact film build by Bi_3YO_6 coarse grains to be obtained. Clearly visible pores between the grains were formed during

CO_2 evolution during thermal degradation of the binder (PEO). The grain size determined using the SEM technique is in the range between about 500 and 2500 nm.

XRD

The XRD patterns of Bi_3YO_6 for the powder sample and the deposited layer are presented in Fig. 2. Both patterns were collected at room temperature and consist of a set of peaks at the same positions. All peaks in the diffraction patterns can be indexed on a cubic Fm-$3m$ cell, with no evidence for phase separation. The preservation of the cubic form after the deposition procedure can be concluded. Structure refinement was carried out by Rietveld fitting of X-ray data set using the program GSAS [29]. For the cubic phase, a fluorite model in space group Fm-$3m$ was used: Bi, and Y were located on the ideal 4a site (0,0,0), with oxide ions initially distributed over three sites: 8c at (0.25, 0.25, 0.25); 32f at approximately (0.3, 0.3, 0.3), and 48i at around (0.5, 0.2, 0.2). A total oxide ion occupancy constraint was applied. Calculated unit cell dimension is 5.49458(9) Å.

ATR FT-IR

Samples of the material in the form of a layer and powder were compared using ATR FT-IR spectroscopy. Spectra of Bi_3YO_6 are characterized by a very intensive peak below 750 cm^{-1} wavenumbers (see Fig. 3), which is characteristic for metal-oxygen vibrations [30]. In the case of the Bi_3YO_6 layer, additional low intensity peaks at 832 and 857, 1112, 1399, and 1497 cm^{-1} were recorded. Two peaks in the 830–860 cm^{-1} range are probably related to O–H deformation vibrations of different bonded OH groups. The peak near 860 cm^{-1} was previously described in the Y_2O_3-B_2O_3-Bi_2O_3 system as [BiO$_3$] unit vibrations [31] and the Bi–O vibration in distorted BiO$_6$ units [32]; however, such peak was not recorded for the material in the form of powder. The peak at 1112 cm^{-1} may originate from C–O–C stretching vibrations as the residue of

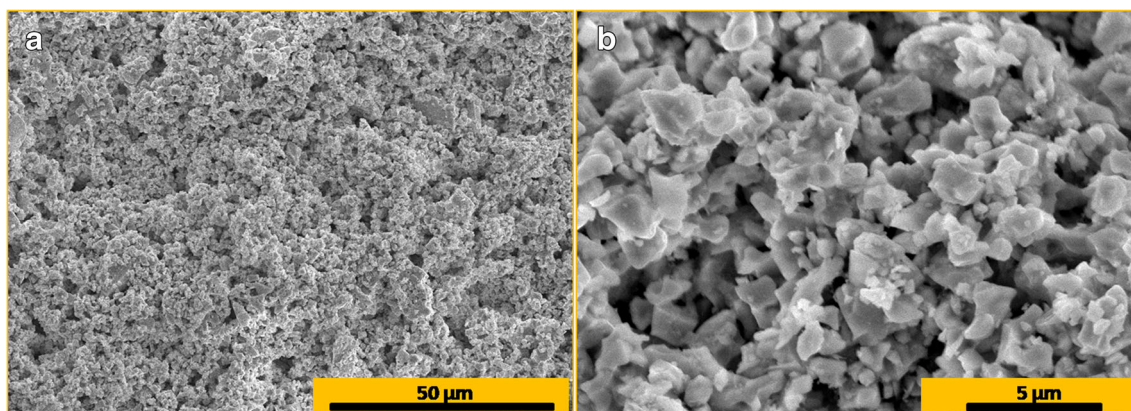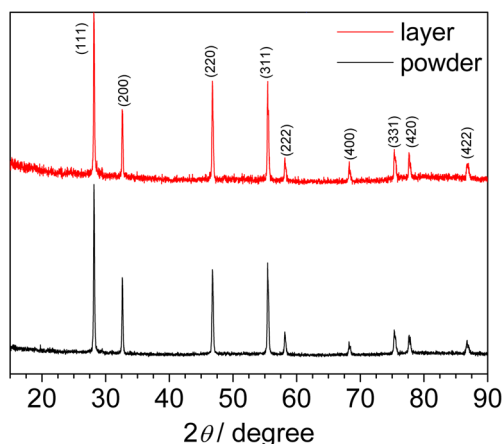**Fig. 1** Scanning electron micrographs of Bi_3YO_6 layers deposited onto the Pt substrate using the dip-coating method

Fig. 2 XRD patterns of Bi_3YO_6 for the powder sample and deposited layer

the binder, and peaks in the range between 1400 and 1500 cm^{-1} could be described as C–H deformation vibrations, but no C–H stretching vibrations near 3000 cm^{-1} were recorded. Additionally, a broad, low intensity band at 3000–3500 cm^{-1} from O–H stretching vibrations was found. The IR spectrum of PEO is presented for comparison. As it may be concluded, all peaks recorded for the Bi_3YO_6 layer in the range between 750 and 1650 cm^{-1} originate from the binder used. Even after prolonged annealing, residues of organic polymer remain on the surface of the deposited material. To sum up, the crystal structure of the material remains unchanged, but the surface of Bi_3YO_6 is slightly modified due to contact with PEO during layer annealing.

UV-Vis spectroscopy

Optical properties of Bi_3YO_6 were examined using UV-Vis spectroscopy in the reflectance mode. Spectra of both samples (powder and layer) are presented in Fig. 4a. Absorption starts at about ~650 nm and has a maximum at ~405 nm. The material absorbs a significant part of visible light, which is a good characteristic of materials that may be used in
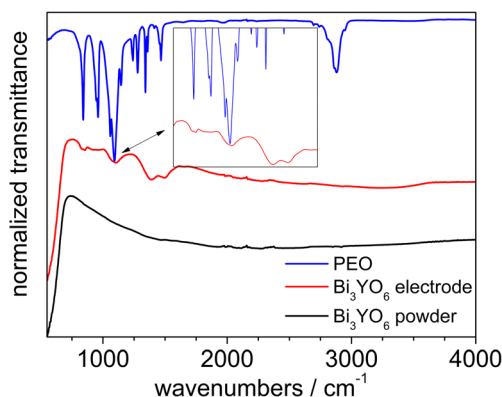

Fig. 3 The comparison of ATR FT-IR spectra of PEO, Bi_3YO_6 powder, and Bi_3YO_6 layer

photocatalysis. The Kubelka-Munk function (Eq. 3) [33] was applied to determine the energy band gap of the tested material.

$$f(KM) = \frac{(1-R)^2}{2R} \tag{3}$$

The energy band gap was determined by extrapolation of the linear region of $(f(KM)\,h\nu)^n$ vs. $h\nu$ and taking an intercept on the x axis. The power "n" is dependent on the type of electron transition ($n = 2$—direct allowed (d.a.), $n = 0.5$—indirect allowed (i.a.), $n = 2/3$—direct forbidden (d.f.), $n = 1/3$—indirect forbidden (i.f.)) [34]. All possibilities (direct and indirect, allowed and forbidden) for the material in the form of powder are shown in Fig. 4b, c (differences between powders and layers were negligible as presented in Fig. S1 in
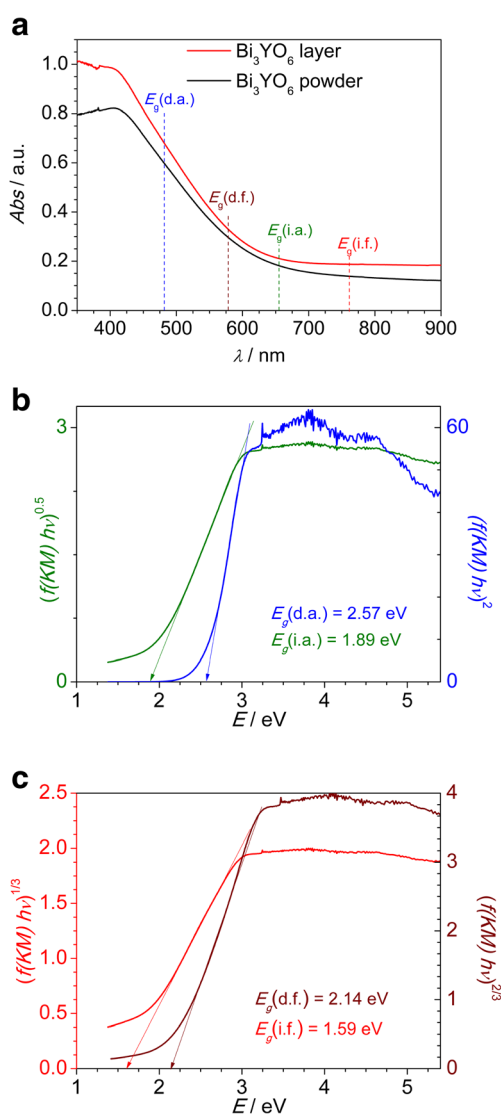
Fig. 4 **a** UV-Vis spectra of Bi_3YO_6 layer and powder. Inset: The photograph of Bi_3YO_6 powder. **b** $(f(KM)\,h\nu)^2$ and $(f(KM)\,h\nu)^{0.5}$ vs. $h\nu$ plots and **c** $(f(KM)\,h\nu)^{1/3}$ and $(f(KM)\,h\nu)^{2/3}$ vs. $h\nu$ plots resulting from the UV-Vis spectrum of Bi_3YO_6 powder

supporting information). The linear region of $(f(KM) \cdot h\nu)^n$ vs. $h\nu$ function can be found in all cases. The estimated values of energy band gaps for each case are marked with an appropriate color on the UV-Vis spectrum in Fig. 4a. There are materials which exhibit two types of transitions [35, 36]. However, taking into account the UV-Vis spectrum in Fig. 4a, absorption starts to rise near 656 nm, which is the value that corresponds to 1.89 eV. Thus, it is very likely that the optical band gap of tested material is related to the allowed indirect transition. The determined value of an energy band gap allowing visible light absorption makes Bi_3YO_6 interesting from the photocatalytical point of view. Nevertheless, optical properties of the studied material should be further examined to describe them in more detail.

The energy band gap of tested material has been also determined using semi-empirical PM7 calculations under LS (Singlet) Born–von Kärmän periodic boundary conditions [37] implemented in MOPAC2016, Version: 17.119W package by James J. P. Stewart [38] at experimental geometry of cubic δ-type phase of $a = 5.496$ Å. Surprisingly, the calculated value of E_g of Bi_3YO_6 is equal to 3.38 eV. This value is 1.49 eV higher than the value of the indirect gap determined from the UV-Vis spectrum. The average unsigned error of PM7 calculated ionization energy in sets of reference compounds (http://openmopac.net/PM7_accuracy/molecules.html) is 0.55 eV. Such a big difference between determined values may then result from the surface properties of Bi_3YO_6. Exclusion of the influence of absorption by impurities or surface electronic states cannot be unambiguously done [39]. For example, as it was previously shown for yttrium-doped $BiVO_4$ ($Bi_xY_{1-x}VO_4$), a surface of bismuth-containing metal oxide is mainly built by BiO_y units [40]. Their presence allows the part of visible light to be absorbed; however, the bulk material is characterized by a different electronic structure and absorbs only UV light.

Electrode characterization

Electrochemical properties

Cyclic voltammetry curves of Pt/Bi_3YO_6 polarization in contact with aqueous electrolytes are presented in Fig. 5. Figure 5a consists of CV curves recorded in 0.1 M K_2SO_4 using different scan rates (10–100 mV s^{-1}). The peak "A" is characteristic for metal oxides electrodes and is associated with the anodic plateau "B." The mentioned electroactivity is related to the surface species present on the hydrated surface of the material, which is in contact with water [41]. Similar processes were observed for titanium dioxide electrodes in previous reports [42, 43]. Anodic peaks marked as "C" and the cathodic peak "D" are characteristic for Bi_3YO_6. The anodic current density maximum shows a linear relation with the scan rate (see Fig. 5b). Interestingly, the current density of the

cathodic peak shows a linear relation with the square root of the scan rate, suggesting process control by diffusion (Fig. 5c). Some of metal oxides exhibit cathodic electroactivity (diffusion controlled) in aqueous electrolytes related to the cation insertion to the oxide structure, e.g., MnO_2 [44]. Additional tests were performed in electrolytes containing various cations (Li^+, Na^+, K^+, Cs^+). CV curves are presented in Fig. 5d. As it can be seen, the size of the cation does not affect the cathodic current density; thus, the observed process is not related to the ion insertion into Bi_3YO_6. The ex-situ measured XRD pattern (see Fig. S2 in supporting information) of the cathodically polarized electrode is the same as for the electrode before electrochemical tests, so electrochemical polarization does not affect the crystal structure of the studied material. Peaks observed on the CV curve are probably related to the surface group activity. Noteworthy, similar peaks were recorded in 0.2 M KNO_3 but were not recorded during electrode polarization, which was immersed in a chloride-containing electrolyte (0.2 M KCl) as it is shown in Fig. 5e. The presence of Cl^- anions in the electrolyte which adsorb on the electrode surface deactivates electroactive groups on the surface of Bi_3YO_6. The cathodic current recorded at ~ -0.8 V is related to the irreversible reduction of the material in KCl aqueous electrolyte. Long-term cathodic polarization of Bi_3YO_6 in KCl aqueous electrolyte leads to layer darkening. Two small peaks recorded when the electrode was polarized in the anodic direction may be related to partial two-step oxidation of metallic bismuth [45].

The electroactivity recorded in sulfate- and nitrate-containing electrolytes is not related to the surface groups observed on the FT-IR spectrum and formed during layer preparation. An additional cyclic voltammetry curve was recorded for the electrode prepared without PEO (using a glass capillary filled with Bi_3YO_6 and a platinum wire as the electrical contact). CV is presented in Fig. 5f. As it can be seen, the shape of the curve is the same as in the case of the electrodes prepared by the dip-coating method; thus, the used method of film deposition does not affect Bi_3YO_6 electroactivity.

The Pt/Bi_3YO_6 was tested as an potential electrode for energy storage devices. The capacitance was calculated from multiple galvanostatic (1 mA cm^{-2}) charge/discharge cycles recorded in 0.1 M K_2SO_4 presented in Fig. 5g. Multiple chronopotentiometry curves allow the electrochemical stability to be tested. The capacitance is relatively stable during the first 6000 cycles and then surprisingly increases reaching the value of 10.5 mF cm^{-2} (~ 500 mF g^{-1}, ~ 2100 mF cm^{-3}) as it is shown in Fig. 5h. It may be related to the penetration of the layer pores with electrolyte. Material started to lose its capacitance after 12,500 cycles which indicates high electrostability of the tested Bi_3YO_6 electrode.

The influences of electrolytes used (K_2SO_4 and KCl) on the electrical properties of the Pt/Bi_3YO_6 electrode and electrode/
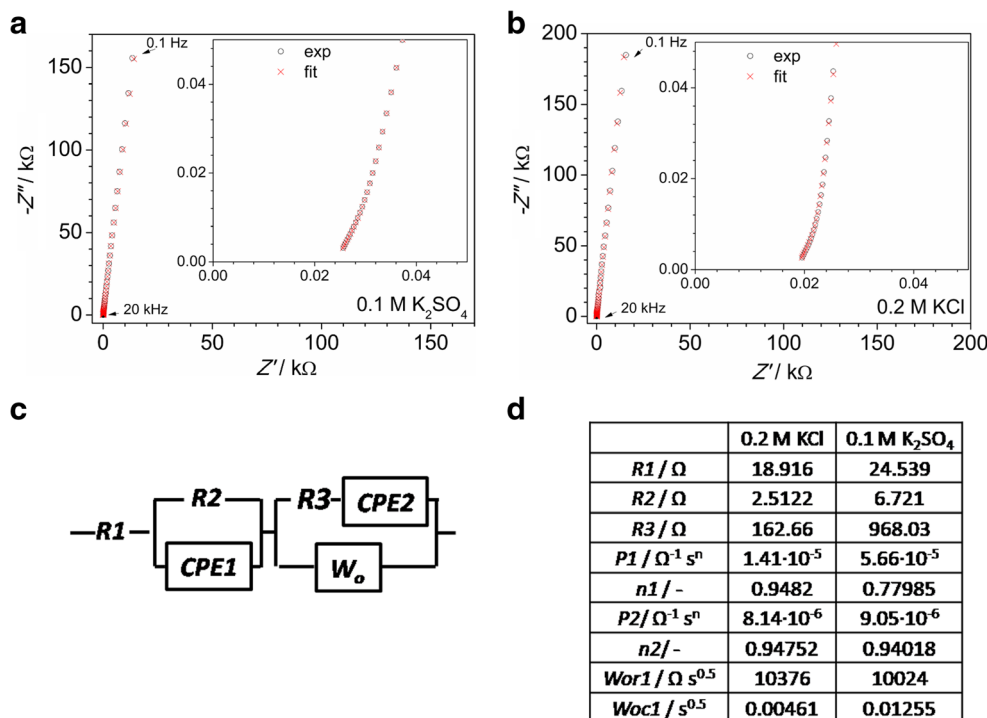
Fig. 5 **a** CV curves of Pt/Bi$_3$YO$_6$ electrode in 0.1 M K$_2$SO$_4$. Scan rates 10–100 mV s^{-1}. Dependence of current density of anodic and cathodic maxima **b** vs. scan rate and **c** vs. square root of the scan rate. **d** CV curves of Pt/Bi$_3$YO$_6$ electrodes registered in different electrolytes (Li$_2$SO$_4$, Na$_2$SO$_4$, K$_2$SO$_4$, and Cs$_2$SO$_4$ (scan rate—100 mV s^{-1}). **e** The comparison of CV curves of Pt/Bi$_3$YO$_6$ recorded in KNO$_3$ and KCl (scan rate—100 mV s^{-1}). **f** CV curve of Bi$_3$YO$_6$ electrode prepared without polyethylene oxide (scan rate—100 mV s^{-1}). **g** The chronopotentiometry curves ($j_c = j_a = 1$ mA cm^{-2}). **h** Resulting capacitance vs. number of cycle plot
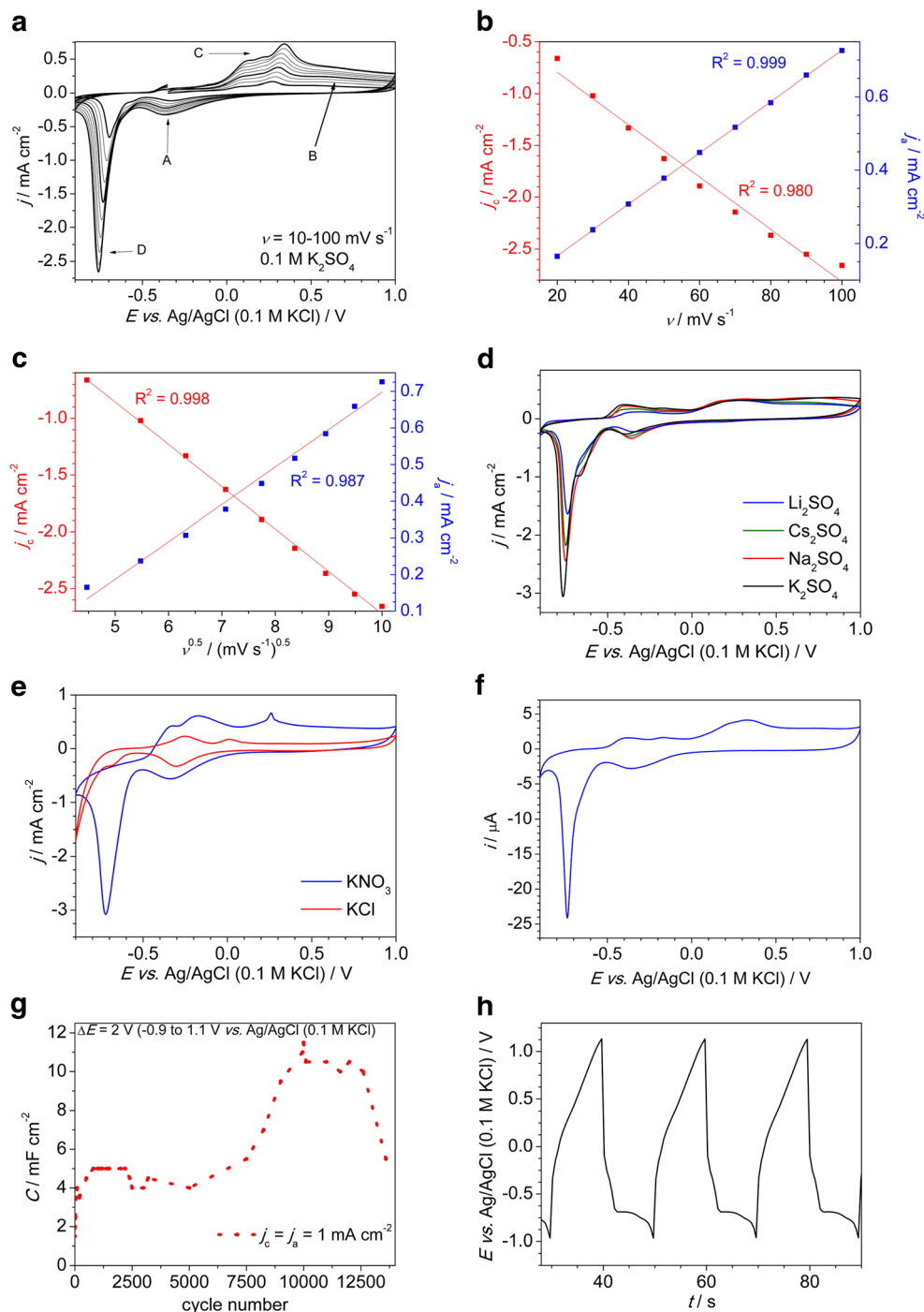
electrolyte interface were investigated using electrochemical impedance spectroscopy. The impedance spectra recorded in both electrolytes were recorded at rest potential and are shown in Fig. 6a, b. As it is presented, the spectra are very similar. A fitting procedure using the equivalent circuit (EQC) presented in Fig. 6c was performed. The EQC consists of six elements as it is shown in Fig. 6c. The *R1* resistor represents the electrolyte and external contact resistance. The constant phase element (*CPE1*) and resistor *R2* are probably related with charge

transfer at the electrolyte/electrode interface. The second constant phase element (*CPE2*) connected in parallel with resistor *R3* and Warburg element (*W$_o$*) can be interpreted as related to the grain boundary resistance and diffusion in pores. It is consistent with the morphology of the film as it is presented on the SEM micrographs (see Fig. 1). The results of the fitting procedure in the form of table are presented in Fig. 6. As it may be concluded, the "bulk" properties of the electrode (elements *R3* and *CPE2*) do not change significantly with the electrolyte

Fig. 6 The registered "o" and fitted "x" impedance spectra of Pt/Bi$_3$YO$_6$ electrode recorded in **a** 0.1 M K$_2$SO$_4$ and **b** 0.2 M KCl at rest potential. **c** The electrical equivalent circuit used in EIS analysis and the table with the obtained results and d values of parameters of equivalent circuit

	0.2 M KCl	0.1 M K$_2$SO$_4$
R1 / Ω	18.916	24.539
R2 / Ω	2.5122	6.721
R3 / Ω	162.66	968.03
P1 / Ω^{-1} s^n	1.41·10^{-5}	5.66·10^{-5}
n1 / -	0.9482	0.77985
P2 / Ω^{-1} s^n	8.14·10^{-6}	9.05·10^{-6}
n2 / -	0.94752	0.94018
Wor1 / Ω s$^{0.5}$	10376	10024
Woc1 / s$^{0.5}$	0.00461	0.01255

used. However, the change of the *R2* and *CPE2* elements is clear. The resistance on the electrolyte/electrode interface is almost six times higher in the case of K$_2$SO$_4$ electrolyte. It can be related to the hydroxylation of the surface of the electrode and formation of surface groups, which is consistent with CV curves recorded in chloride- and sulfate-containing electrolytes. Moreover, the differences of the value of "*P*" parameter in the *CPE2* element indicate changes in the electrical double layer capacitance. Thus, the presence of chlorides affects the electrode/electrolyte interface and affects the electrochemical properties of Pt/Bi$_3$YO$_6$.

XPS analysis

XPS analysis was performed to find changes in chemical surface stages of Bi, Y, and O induced by polarization of the Pt/Bi$_3$YO$_6$ electrodes. In all cases, except the sample after anodic polarization in K$_2$SO$_4$ electrolyte, the energy range characteristic for the O1s orbital was fitted using three oscillators. An exemplary spectrum of a layer is presented in Fig. 7a. The peak at the highest binding energy (530.9 eV) marked as A can be assigned to OH groups as it was shown in the case of other metal oxides [46, 47]. The second one (B) at 528.7 eV is probably observed due to the presence of lattice metal-oxygen bonds [48–50]. The third peak (C) at 526.3 eV may be related to carbon-containing contaminations. Unfortunately, cleaning of the surface using the argon-ion sputtering procedure cannot be applied for these types of samples. The Ar$^+$ beam significantly affects the XPS spectrum in an energy range characteristic for bismuth. The phenomenon of metal reduction due to Ar$^+$ treatment was already observed for other metal oxides, e.g., CuO [51], TiO$_2$ [52, 53], and MoO$_3$ [54]. In the case of electrooxidized samples, an additional peak marked as D at 532.4 eV has been found (see Fig. 7b). It indicates that anodic polarization (0.9 V, 60 min) leads to the formation of oxygen-rich surface groups which are the precursors of oxygen evolution, as it was previously reported for a preilluminated TiO$_2$ photoanode [41]. In the case of the electrooxidized sample, also the relative intensity of the peak A increased significantly suggesting formation of new OH groups on the surface of the electrode.

The doublet characteristic for yttrium 3d orbital overlaps with the signal from Bi 4f, as it is shown in Fig. 7c. After deconvolution of all samples' spectra, positions of peaks at 155.7 eV (A) and 158.1 eV (B) were shifted slightly (± 0.4 eV) between the samples and no new peak characteristic for yttrium appeared after electrochemical treatment. More detailed analysis of the Y 3d orbital is very difficult due to the low intensity of peaks in comparison with overlapping Bi 4f peaks. Polarization of Pt/Bi$_3$YO$_6$ does not clearly affect Y atoms in the samples. However, changes of the peaks coming from the Bi 4f orbital can be found. The intensity and area ratios of the peaks marked as C1 (158.3 ± 0.2 eV), C2 (163.6 ± 0.1 eV), D1 (160.3 ± 0.1 eV), and D2 (165.5 eV) change as it is shown for the samples electrooxidized and electroreduced in K$_2$SO$_4$ electrolyte (see. Fig. 7c, d). Two doublets of the Bi 4f orbital were already reported, e.g., for Bi$_2$O$_{2.33}$ [55] and Bi$_2$WO$_6$ [56], and were interpreted as coexistence of Bi^{3+} and Bi in the lower oxidation states. It may be

Fig. 7 The XPS spectra of the **a** as prepared and **b** anodically polarized Pt/Bi$_3$YO$_6$ in the O1s region. The XPS spectra of the **c** reduced and **d** oxidized Pt/Bi$_3$YO$_6$ electrode in the Bi 4f region
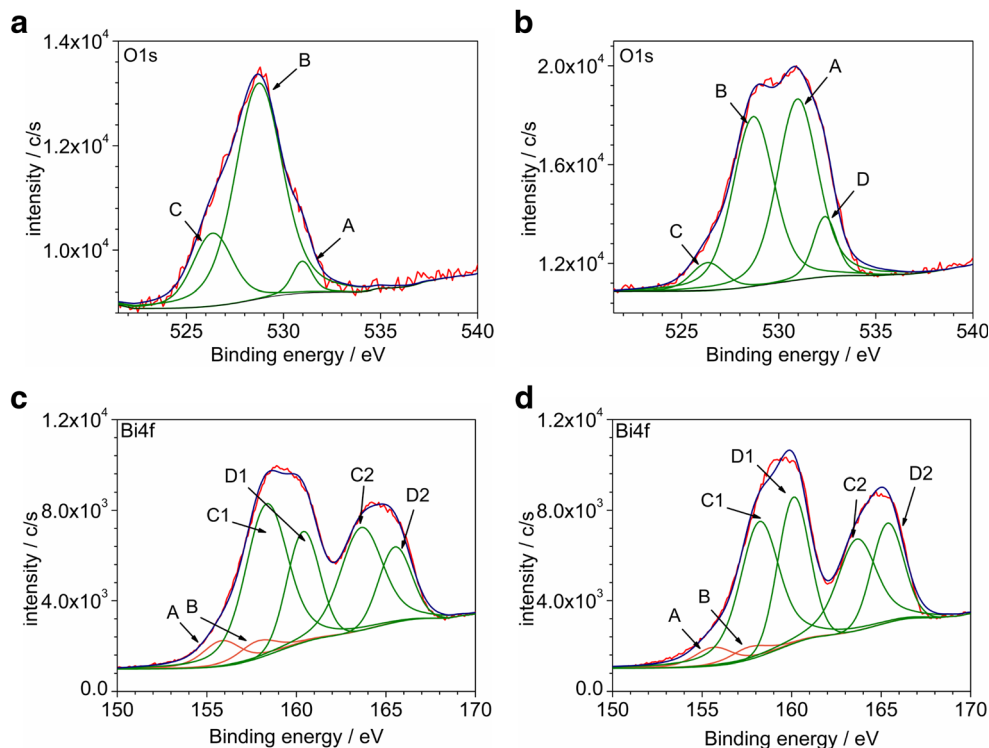
concluded that electroactivity recorded on the cyclic voltammetry curves is related to the changes of Bi species on the surface of the electrode. Thus, cathodic polarization of the electrode leads to the formation of the "Bi suboxides" [57, 58] as the increase of the intensity of the peak related to the reduced form of Bi is observed.

### Photoelectrochemical performance

Photoelectrochemical properties of prepared electrodes were examined using the chronoamperometry technique recorded under intermittent illumination. First, the electrode was polarized ($E = const$) in dark conditions to achieve a steady state current. Then, the electrode was illuminated and the current was measured. In the case of simulated solar light (AM 1.5 filter), the photocurrent was not generated. Despite the material is yellow and exhibits absorption in the visible range of electromagnetic radiation, absorbed photons were not converted to electrical energy. Thus, it is very likely that UV-Vis spectroscopy shows the surface electronic states, but the real, "bulk" energy band gap is higher as it follows from the calculations.

Bi$_3$YO$_6$ exhibited photoactivity, when the electrode was illuminated with whole UV-Vis radiation emitted by the lamp (without AM 1.5 filter). It is in agreement with energy band gap estimated using semi-empirical calculations. The chronoamperometry curves ($E = 0.8$ V vs. Ag/AgCl (0.1 M KCl)) are shown in Fig. 8a. As it can be seen, the Bi$_3$YO$_6$ film generated anodic photocurrent. It is characteristic for n-type

semiconductors that can act as photoanodes [59]. The same experimental setup was used for testing other photoanodic materials like, e.g., bismuth vanadate and titania nanotubes [60], and recorded photocurrent was even several hundred times higher. The Pt/Bi$_3$YO$_6$ electrodes were also prepared without binder to exclude the influence of pyrolyzed PEO residues on the obtained results. The chronoamperometric curve is presented in supplementary information (see Fig. S3). In both cases, namely for electrode prepared with PEO binder and electrode Bi$_3$YO$_6$ without binder, the recorded photocurrent is in the same range. Thus, the usage of binder does not affect the photoelectrochemical performance of Bi$_3$YO$_6$ films.

The photocurrent recorded when the electrode was immersed in KCl and K$_2$SO$_4$ is comparable and is related to water and/or chloride oxidation. Illumination of the electrode which is in contact with KOH leads to an over 20 times higher photocurrent. OH$^-$ anions may act as "hole scavengers" because of a lower potential of O$_2$ evolution in comparison with the water oxidation reaction ($2H_2O \rightarrow O_2 + 4H^+ + 4e^-$, $E = 1.23$ V and $4OH^- \rightarrow O_2 + 2H_2O + 4e^-$, $E = 0.4$ V). The chronoamperometry curves of the Pt/Bi$_3$YO$_6$ electrode at $E = -0.75$ V vs. Ag/AgCl (0.1 M KCl) are presented in Fig. 8b. In the case of the KOH and KCl electrolyte, the effect of photocurrent generation is not clearly observed. However, the electrode immersed in K$_2$SO$_4$ electrolyte generates an anodic photocurrent even at cathodic potential. The n-type semiconductor can act as a photoanode only when the applied potential is higher (more anodic) than the flat band potential (E_{fb}). It
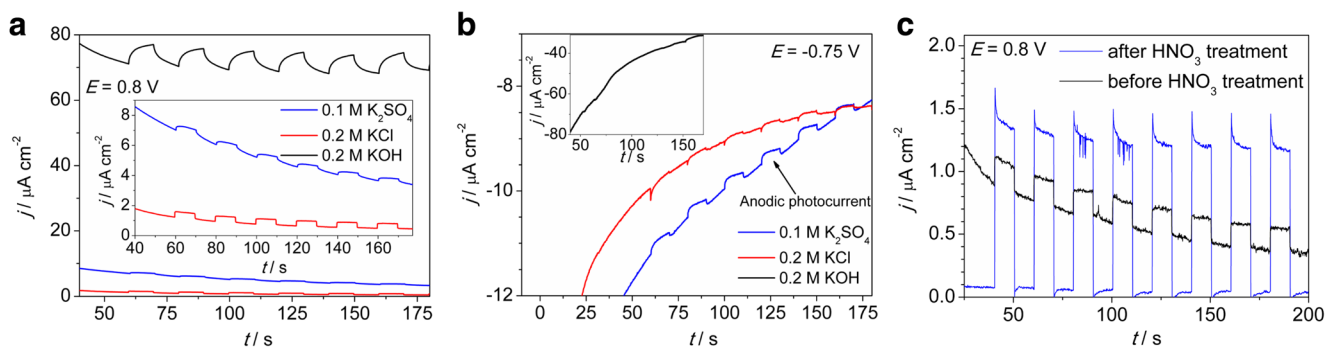
Fig. 8 Chronoamperometry curves of Pt/Bi$_3$YO$_6$ electrode immersed in K$_2$SO$_4$, KCl, and KOH recorded under intermittent UV-Vis illumination at **a** $E = 0.8$ V vs. Ag/AgCl (0.1 M KCl) and **b** $E = -0.75$ V vs. Ag/AgCl (0.1 M KCl). **c** The comparison of CA curves recorded at 0.8 V vs. Ag/AgCl (0.1 M KCl)

means that the E_{fb} is more cathodic than -0.75 V vs. Ag/AgCl (0.1 M KCl); however, the precise value was not evaluated. A routine procedure for E_{fb} evaluation using Mott-Schottky plot is found in the studied case to be ambiguous due to complexity of the electrode/electrolyte interface in a broad potential range. Surface active species give rise to electrochemical capacitance of Pt/Bi$_3$YO$_6$ electrodes as one may see on CV curves (see Fig. 5).

It was reported that photoactivity of bismuth-containing catalysts may be inhibited due to the BiO$_y$ clusters on the surface of the oxide. Differences in the electronic structure of the bulk material and the BiO$_y$-rich surface lead to the adverse "self-heterojunction" formation [40]. The authors proposed a method of BiO$_y$ removing from the surface using diluted HNO$_3$. Almost four times enhancement of photocatalytic water splitting efficiency was observed after HNO$_3$ treatment [40]. In the present work, the same method has been utilized to improve photoelectrocatalytical performance of Bi$_3$YO$_6$. The comparison of chronoamperometry curves recorded during illumination of the Pt/Bi$_3$YO$_6$ photoanode before and after acid treatment is presented in Fig. 8c ($E = 0.8$ V, 0.1 M K$_2$SO$_4$). It is clearly seen that HNO$_3$ treatment leads to photocurrent increase from 0.19 to 1.14 μA cm^{-2}. Thus, acid treatment enhanced not only photocatalytic, but also photoelectrocatalytic properties of Bi-containing metal oxide semiconductors.

may act as a photoanode. An anodic photocurrent was generated in a wide range of applied potentials, proving that the tested material is an n-type semiconductor. It was shown that despite optical energy band gap equals to 1.89 eV, tested material does not generate photocurrent when illuminated with visible light. The electron transition observed on the reflectance spectrum cannot be converted to the photoelectrochemical water oxidation.

The electrode Pt/Bi$_3$YO$_6$ exhibited electrochemical activity related to the changes of the Bi oxidation state when polarized in aqueous electrolytes. However, the reversible cathodic process at $E = -0.75$ V vs. Ag/AgCl (0.1 M KCl), which is controlled by diffusion, was registered only in Cl$^-$-free electrolytes. The influence of electrolyte (KCl and K$_2$SO$_4$) on electrical properties of the electrode/electrolyte interface was investigated using electrochemical impedance spectroscopy. The lower electrical capacitance was observed in the KCl electrolyte.

Conclusions

The influence of the deposition procedure on the Bi$_3$YO$_6$ structure and optical properties was presented. The surface of the deposited layer was slightly changed in comparison with the bulk material, as it was presented in IR spectra. The indirect energy band gap of the tested material was estimated to be 1.89 eV using the Kubelka-Munk function, which is a 1.49 eV lower value than that calculated using semi-empirical PM7 calculations. Photoelectrochemical tests under UV-Vis illumination show that the Bi$_3$YO$_6$ film deposited onto Pt foil

References

1. Barsan N, Koziej D, Weimar U (2007) Metal oxide-based gas sensor research: how to? Sensors Actuators B Chem 121(1):18–35
2. Maruthupandy M, Zuo Y, Chen JS, Song JM, Niu HL, Mao CJ, Zhang SY, Shen YH (2017) Synthesis of metal oxide nanoparticles (CuO and ZnO NPs) via biological template and their optical sensor applications. Appl Surf Sci 397:167–174
3. Nowak AP, Lisowska-Oleksiak A, Siuzdak K, Sawcza M, Gazda M, Karczewski J, Trykowski G (2015) Tin oxide nanoparticles from laser ablation encapsulated in a carbonaceous matrix—a

negative electrode in lithium-ion battery applications. RSC Adv 5(102):84321–84327

4. Siuzdak K, Szkoda M, Sawczak M, Lisowska-Oleksiak A, Karczewski J, Ryl J (2015) Enhanced photoelectrochemical and photocatalytic performance of iodine-doped titania nanotube arrays. RSC Adv 5(62):50379–50391

5. Kiefer W, Mazzolini AP, Stoddart PR (2007) Recent advances in linear and nonlinear Raman spectroscopy I. J Raman Spectrosc 38(12):1538–1553

6. Gujar TP, Shinde VR, Lokhande CD, Han S (2006) Electrosynthesis of Bi_2O_3 thin films and their use in electrochemical supercapacitors. J Power Sources 161(2):1479–1485

7. Khan Z, Battu S, Haram S, Khushalani D (2014) SWCNT/$BiVO_4$ composites as anode material for supercapacitor application. RSC Adv 4(33):17378–17381

8. Trzciński K, Borowska-Centkowska A, Sawczak M, Lisowska-Oleksiak A (2015) Photoelectrochemical properties of BIMEVOX (ME=Cu, Zn, Mn) electrodes in contact with aqueous electrolyte. Solid State Ionics 271:63–68

9. Zhang L, Xu T, Zhao X, Zhu Y (2010) Controllable synthesis of Bi_2MoO_6 and effect of morphology and variation in local structure on photocatalytic activities. Appl Catal B Environ 98(3-4):138–146

10. Weng SX, Chen BB, Xie LY, Zheng Z, Liu P (2013) Facile in situ synthesis of a Bi/BiOCl nanocomposite with high photocatalytic activity. J Mater Chem A 1(9):3068–3075

11. Li J, Zhang X, Ai Z, Jia F, Zhang L, Lin J (2007) Efficient visible light degradation of rhodamine B by a photo-electrochemical process based on a Bi_2WO_6 nanoplate film electrode. J Phys Chem 111:6832–6836

12. Takahashi T, Iwahara H, Nagai Y (1972) High oxide ion conduction in sintered Bi_2O_3 containing SrO, CaO or La_2O_3. J Appl Electrochem 2(2):97–104

13. Sammes NM, Tompsett GA, Näfe H, Aldinger F (1999) Bismuth based oxide electrolytes—structure and ionic conductivity. J Eur Ceram Soc 19(10):1801–1826

14. Takahshi T, Iwahara H, Arao T (1975) High oxide ion conduction in sintered oxides of the system Bi_2O_3-Y_2O_3. J Appl Electrochem 5(3):187–195

15. Krynski M, Wrobel W, Dygas JR, Wrobel J, Malys M, Śpiewak P, Kurzydlowski KJ, Krok F, Abrahams I (2013) Ab-initio molecular dynamics simulation of δ-Bi_3YO_6. Solid State Ionics 245–246:43–48

16. Abrahams I, Liu X, Hull S, Norberg ST, Krok F, Kozanecka-Szmigiel A, Islam MS, Stokes SJ (2010) A combined total scattering and simulation approach to analyzing defect structure in Bi_3YO_6. Chem Mater 22(15):4435–4445

17. Krynski M, Wrobel W, Mohn CE, Dygas JR, Malys M, Krok F, Abrahams I (2014) Trapping of oxide ions in δ-Bi_3YO_6. Solid State Ionics 264:49–53

18. Abrahams I, Krok F, Kozanecka-Szmigiel A, Wrobel W, Chan SCM, Dygas JR (2007) Effects of ageing on defect structure in the Bi_3NbO_7-Bi_3YO_6 system. J Power Sources 173(2):788–794

19. Liu X, Abrahams I, Hull S, Norberg ST, Holdynski M, Krok F (2011) A neutron total scattering study of defect structure in $Bi_3Nb_{0.5}Y_{0.5}O_{6.5}$. Solid State Ionics 192(1):176–180

20. Borowska-Centkowska A, Leszczynska M, Wrobel W, Malys M, Krynski M, Hull S, Krok F, Abrahams I (2017) Structure and conductivity in tungsten doped δ-Bi_3YO_6. Solid State Ionics 308:61–67

21. Pasciak G, Prociow K, Mielcarek W, Gornicka B, Mazurek B (2001) Solid electrolytes for gas sensors and fuel cells applications. J Eur Ceram Soc 21(10-11):1867–1870

22. Boivin JC, Pirovano C, Nowogrocki G, Mairesse G, Labrune PH, Lagrange G (1998) Electrode–electrolyte BIMEVOX system for moderate temperature oxygen separation. Solid State Ionics 113–115:639–651

23. dos Santos WS, Rodriguez M, Afonso AS, Mesquita JP, Nascimento LL, Patrocinio AOT, Silva AC, Oliveira LCA, Fabris JD, Pereira MC (2016) A hole inversion layer at the $BiVO_4$/$Bi_4V_2O_{11}$ interface produces a high tunable photovoltage for water splitting. Sci Rep 6(1):31406

24. dos Santos WS, Almeida LD, Afonso AS, Rodriguez M, Mesquita JP, Monteiro DS, Oliveira LCA, Fabris JD (2016) Photoelectrochemical water oxidation over fibrous and sponge-like $BiVO_4$/β-$Bi_4V_2O_{11}$ photoanodes fabricated by spray pyrolysis. Appl Catal B Environ 182:247–256

25. Bhat SSM, Won H (2017) Recent advances in bismuth based materials for photoelectrochemical water splitting. ChemSusChem 10(15):3001–3018

26. Xie W, Qin N, Li B, Bao D (2015) Enhanced visible-light catalytic activity of Au nanoparticles loaded c-axis oriented $Bi_2VO_{5.5}$ porous thin films. Ceram Int 41:1–11

27. Chen X, Liu J, Wang H, Ding Y, Sun Y, Yan H (2013) One-step approach to novel $Bi_4V_2O_{11}$ hierarchical hollow microspheres with high visible-light-driven photocatalytic activities. J Mater Chem A 1(3):877–883

28. Lv C, Chen G, Sun J, Zhou Y (2016) Construction of α-β phase junction on $Bi_4V_2O_{11}$ via electrospinning retardation effect and its promoted photocatalytic performance. Inorg Chem 55(10):4782–4789

29. Larson AC, Von Dreele RB (1987) Los Alamos National Laboratory report LA-10160-MS. No. LAUR-86-748

30. Wachs IE (1996) Raman and IR studies of surface metal oxide species on oxide supports: supported metal oxide catalysts. Catal Today 27(3-4):437–455

31. Simon S, Eniu D (2007) Spectroscopic characterisation of local structure in Y_2O_3–B_2O_3–Bi_2O_3 glasses doped with gadolinium. J Mater Sci 42(15):5949–5953

32. Pascuta P, Culea E (2008) FTIR spectroscopic study of some bismuth germanate glasses containing gadolinium ions. Mater Lett 62(25):4127–4129

33. Barron V, Torrent J (1986) Use of the Kubelka-Munk theory to study the influence of iron oxides on soil colour. J Soil Sci 37(4):499–510

34. López R, Gómez R (2012) Band-gap energy estimation from diffuse reflectance measurements on sol-gel and commercial TiO_2: a comparative study. J Sol-Gel Sci Technol 61(1):1–7

35. Cooper JK, Gul S, Toma FM, Chen L, Liu YS, Guo J, Ager JW, Yano J, Sharp ID (2015) Indirect bandgap and optical properties of monoclinic bismuth vanadate. J Phys Chem C 119(6):2969–2974

36. Trzciński K, Gasiorowski J, Borowska-Centkowska A, Szkoda M, Sawczak M, Hingerl K, Zahn DRT, Lisowska-Oleksiak A (2017) Optical and photoelectrochemical characterization of pulsed laser deposited $Bi_4V_2O_{11}$, BICUVOX, and BIZNVOX. Thin Solid Films 638:251–257

37. Stewart JJP (2013) Optimization of parameters for semiempirical methods VI: more modifications to the NDDO approximations and re-optimization of parameters. J Mol Model 19(1):1–32

38. Stewart Computational Chemistry. http://openmopac.net

39. Ohtani B (2010) Photocatalysis A to Z—what we know and what we do not know in a scientific sense. J Photochem Photobiol C Photochem Rev 11(4):157–178

40. Fang W, Liu J, Yang D, Wei Z, Jang Z, Shangguan W (2017) Effect of surface self-heterojunction existed in $Bi_xY_{1-x}VO_4$ on photocatalytic overall water splitting effect of surface self-heterojunction existed in $Bi_xY_{1-x}VO_4$ on photocatalytic overall water splitting. ACS Sustain Chem Eng 5(8):6578–6584

41. Augustynski J (1988) Aspects of photo-electrochemical and surface behaviour of titanium(IV) oxide. Solid Mater 69:1–61

42. Szybowska K, Lisowska-Oleksiak A (2011) On stability of iodine doped TiO_2 electrodes in pH varied aqueous electrolytes. Solid State Ionics 188(1):165–169

43. Trzciński K, Lisowska-Oleksiak A (2015) Electrochemical characterization of a composite comprising PEDOT/PSS and N doped TiO_2 performed in aqueous and non-aqueous electrolytes. Synth Met 209:399–404

44. Cheng S, Yang L, Chen D, Ji X, Jiang ZJ, Ding D, Lie M (2014) Phase evolution of an alpha MnO_2-based electrode for pseudocapacitors probed by in operando Raman spectroscopy. Nano Energy 9:161–167. https://doi.org/10.1016/j.nanoen.2014.07.008

45. Sarma B, Jurovitzki AL, Smith YR, Mohanty SK, Misra M (2013) Redox-induced enhancement in interfacial capacitance of the titania nanotube/bismuth oxide composite electrode. ACS Appl Mater Interfaces 5(5):1688–1697

46. Jia Q, Iwashina K, Kudo A (2012) Facile fabrication of an efficient $BiVO_4$ thin film electrode for water splitting under visible light irradiation. PNAS 109(29):11564–11569

47. McCafferty E, Wightman JP (1998) Determination of the concentration of surface hydroxyl groups on metal oxide films by a quantitative XPS method. Surf Interface Anal 564:549–564

48. Peng S, Li L, Zhu P, Wu Y, Srinivasan M, Mhaisalkar SG, Ramakrishna S, Yan Q (2013) Controlled synthesis of BiOCl hierarchical self-assemblies with highly efficient photocatalytic properties. Chem Asian J 8(1):258–268

49. Wang M, Che Y, Niu C, Dang M, Dong D (2013) Effective visible light-active boron and europium co-doped $BiVO_4$ synthesized by sol-gel method for photodegradion of methyl orange. J Hazard Mater 262:447–455

50. Kang S, Pawar RC, Khare V, Lee CS (2015) Size-controlled BiOCl–RGO composites having enhanced photodegradative properties. J Exp Nanosci 11:259–275

51. Panzner G, Egert B, Schmidt HP (1985) The stability of CuO and Cu_2O surfaces during argon sputtering studied by XPS and AES. Surf Sci 151(2-3):400–408

52. Hashimoto S, Tanaka A (2002) Alteration of Ti 2p XPS spectrum for titanium oxide by low-energy Ar ion bombardment. Surf Interface Anal 34(1):262–265

53. Bardi U, Tamura K, Owari M, Nihei Y (1988) Angular resolved X-ray photoemission study of defects induced by ion bombardment on the TiO_2 surface. Appl Surf Sci 32(4):352–362

54. Kim KS, Baitinger WE, Amy JW, Winograd N (1974) ESCA studies of metal-oxygen surfaces using argon and oxygen ion-bombardment. J Electron Spectros Relat Phenomena 5(1):351–367

55. Guan H, Zhang X, Xie Y (2014) Soft-chemical synthetic nonstoichiometric $Bi_2O_{2.33}$ nanoflower: a new room-temperature ferromagnetic semiconductor. J Phys Chem C 118(46):27170–27174

56. Wu L, Bi J, Li Z, Wang X, Fu X (2008) Rapid preparation of Bi_2WO_6 photocatalyst with nanosheet morphology via microwave-assisted solvothermal synthesis. Catal Today 131(1-4):15–20

57. Jiang X, Su L, Yu P, Guo X, Tang H, Xu X, Zheng L, Li H, Xu J (2013) Broadband photoluminescence of Bi_2O_3–GeO_2 binary systems: glass, glass-ceramics and crystals. Laser Phys 23(10):105812

58. Dharmadhikari VS, Sainkar SR, Badrinarayan S, Goswami A (1982) Characterisation of thin films of bismuth oxide by X-ray photoelectron spectroscopy. J Electron Spectros Relat Phenomena 25(2):181–189

59. Bott AW (1998) Electrochemistry of semiconductors. Curr Sep 3:87–91

60. Trzciński K, Szkoda M, Siuzdak K, Sawczak M, Lisowska-Oleksiak A (2016) Electrochemical and photoelectrochemical characterization of photoanodes based on titania nanotubes modified by a $BiVO_4$ thin film and gold nanoparticles. Electrochim Acta 222:421–428